

The soft-mode phonons mediated unconventional superconductivity in monolayer 1T'-WTe₂

Wei Yang,¹ Shi-Bin Fu,¹ Yu Yang,² Fa-Wei Zheng,² Xiao-Hui
Wang,¹ Yuan-An Liu,¹ Ning Hao,^{3,*} and Ping Zhang^{2,4,5,†}

¹*Beijing Key Laboratory of Work Safety Intelligent Monitoring,*

Beijing University of Posts and Telecommunications, Beijing 100876, China

²*Institute of Applied Physics and Computational Mathematics, Beijing 100088, China*

³*Anhui Province Key Laboratory of Condensed Matter Physics at Extreme Conditions,
High Magnetic Field Laboratory, Chinese Academy of Sciences, Hefei, 230031, China*

⁴*School of Physics and Physical Engineering,*

Qufu Normal University, Qufu 273165, China

⁵*Beijing Computational Science Research Center, Beijing 100084, China*

Abstract

Recent experiments have tuned the monolayer 1T'-WTe₂ to be superconducting by electrostatic gating. Here, we theoretically study the phonon-mediated superconductivity in monolayer 1T'-WTe₂ via charge doping. We reveal that the emergence of soft-mode phonons with specific momentum is crucial to give rise to the superconductivity in electron-doping regime, whereas no such soft-mode phonons and no superconductivity emerge in hole-doping regime. We also find a superconducting dome, which can be attributed to the change of Fermi surface nesting condition as electron doping. By taking into account the experimentally established strong anisotropy of temperature-dependent upper critical field H_{c2} between the in-plane and out-of-plane directions, we show that the superconducting state probably has the unconventional equal-spin-triplet pairing in A_u channel of C_{2h} point group. Our studies provide a promising understanding to the doping dependent superconductivity and strong anisotropy of H_{c2} in monolayer 1T'-WTe₂.

*Electronic address: haon@hmfl.ac.cn

†Electronic address: zhang_ping@iapcm.ac.cn

Tuning the topological materials to be superconducting provides a highly efficient way to search and study the exotic superconductivity such as unconventional and topological superconductivity. Some methods have been developed to achieve the target, including the doping through metal intercalation [1–4], high pressure [5, 6], proximity effect [7–10], hard and soft tip contact [11–15], and electrostatic gating [16, 17]. Among them, the electrostatic gating has advantage to freely tune the materials in both electron- and hole-doped regimes without introducing dopant. Recently, the intrinsic superconductivity in the monolayer topological insulator $1T'$ -WTe₂ have been experimentally observed by two groups through moderate electrostatic gating [16, 17]. It is found that the superconductivity shows some interesting features. For instance, only the electron-doped regime show the superconductivity with the transition temperature (T_c) up to 1 K, whereas no superconducting signature is observed in the hole-doped regime. Furthermore, the upper critical field H_{c2} shows strong anisotropy between the in-plane $H_{c2,\parallel}$ and out-of-plane $H_{c2,\perp}$, and $H_{c2,\parallel}$ is significantly larger and four times the Pauli paramagnetic limit $1.84T_c$. However, such features have not been comprehensively understood.

In this work, we show that the phonon spectrum of $1T'$ -WTe₂ dramatically softens in the electron-doped regime, but slightly stiffens in the hole-doped regime through density functional calculations. According to the phonon-mediated superconductivity theory, we reveal that the softening of the phonons with specific momentum in electron-doped regime is the driving force to give rise to the superconductivity. We also find an optimal electron-doped concentration, beyond which, the T_c becomes to decline in accompany with the latent charge density wave instability. Thus, there exists a superconducting dome in the phase diagram. Based on the symmetry classification and linearized gap equations, we find that all the pairing channels with specific irreducible representations (IRs) are degenerate without external magnetic field. However, only the pairing in A_u channel shows the experimentally observed reasonable anisotropy between $H_{c2,\parallel}$ and $H_{c2,\perp}$. This behavior indicates that the superconductivity in $1T'$ -WTe₂ probably has equal-spin-triplet pairing and belongs to unconventional type.

Figure 1 shows the electronic structure of $1T'$ -WTe₂ in the electron-doped and hole-doped regimes. Around the Fermi surface, the d orbitals of W and p orbitals of Te are dominated. Along $\Gamma - X$ line, there are two electron pockets labeled by K' and K in electron-doped case while only one hole pocket centered at Γ point in hole-doped case. The charge doping

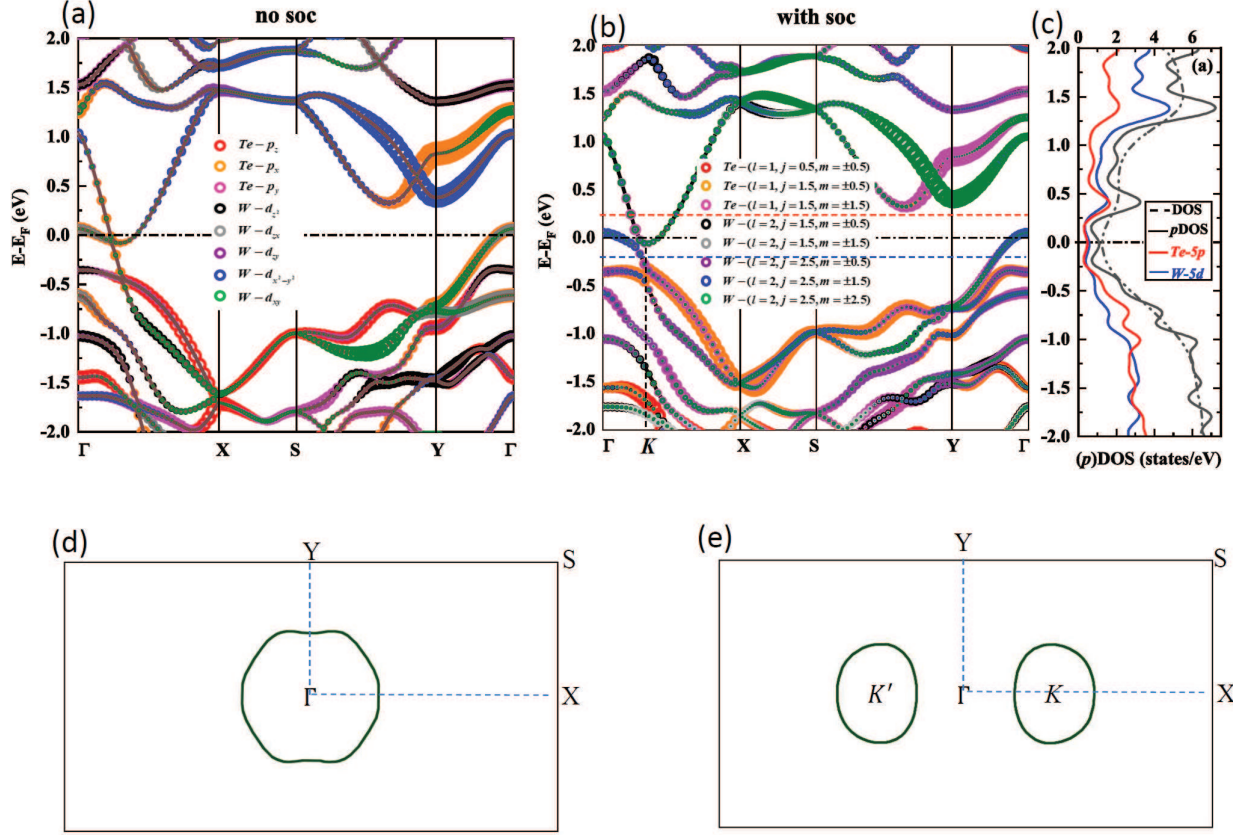


FIG. 1: (Color online)(a) and (b) The orbital-resolved band structures of $1T'$ -WTe along the high-symmetry lines without and with spin-orbit coupling, respectively. The weight of the orbital is labeled by the linewidth. In (b), the conduction band bottom is labeled by $K = (\frac{17}{50}, 0)$ in units $\frac{2\pi}{a}$ and $\frac{2\pi}{b}$ ($a = 3.49\text{\AA}$ and $b = 6.31\text{\AA}$ are the lattice constants [18]). (c) The density of states of band structure with spin-orbit coupling. (d) and (e) the Fermi surfaces for the hole- and electron-doping cases with the Fermi levels labeled by the blue-dashed and red-dashed lines in (b), respectively.

effect is simulated by adding or removing electrons to the monolayer $1T'$ -WTe₂ with a compensating uniform charge background. The level of doped carrier concentrations per $1T'$ -WTe₂ is expressed as n (cm⁻²), with positive and negative values indicating electron and hole doping, respectively.

The calculated phonon spectra of doped $1T'$ -WTe₂ at different doping levels are shown in Figs. 2(a)-(c). Remarkably, some phonon modes at specific wave vectors Q and Q_1 dramatically soften at electron-doped regime in Fig. 2(c), but slightly stiffen at hole doping in Fig. 2(a). As shown in Fig. 2(d), the frequency ω_Q of acoustic phonon branch involving

Q mode manifests significant asymmetry between electron doping and hole doping. The Q -mode phonon is softened in electron doping and the softening is enhanced as doping density increases. As shown in the inset in Fig. 2(d), the frequency of the Q mode phonon turns to be negative when $|n_e|$ crosses $10.3 \times 10^{13} \text{ cm}^{-2}$. It indicates that some long-range order instability could emerge. In the present case, such instability is probably the charge density wave. Furthermore, the relevant atomic displacements for the Q mode phonon are mainly expressed as horizontal W-W stretching vibration and shear Te-Te tortuosing vibration, as shown in Figs. 2(e)-(g). These behaviors indicate the Q mode phonon has the longitudinal-wave feature. We have checked that the properties of Q_1 mode phonon are similar to those of the Q mode phonon.

The spectral features in Fig. 2 imply that the soft mode phonons should play a key role in the electron-hole doping asymmetry of superconductivity in monolayer 1T'-WTe₂. To prove it, we also plot the linewidth of the phonon spectra $\gamma_{q,\nu}$ shown in Figs. 2(a)-(c). The Eliashberg spectral function $\alpha^2 F(\omega)$ can be calculated by [19]

$$\alpha^2 F(\omega) = \frac{1}{N_0 \pi} \sum_{q,\nu} \frac{\gamma_{q,\nu}}{\omega_{q,\nu}} \delta(\omega - \omega_{q,\nu}), \quad (1)$$

where N_0 is the electronic density of states at the Fermi surface for both spin orientations and $\omega_{q,\nu}$ is the phonon spectrum with momentum q and mode index ν . Considering the total electron-phonon coupling (EPC) constant $\lambda^{ph} = 2 \int_0^\infty \alpha^2 F(\omega) / \omega d\omega$, the momentum, frequency and mode resolved EPC $\lambda_{q,\nu}^{ph}(\omega) = 4\gamma_{q,\nu} / (N_0 \pi \omega^2) \delta(\omega - \omega_{q,\nu})$. In terms of superconductivity, only the electrons very close to the Fermi surface need to be considered. It requires the energy difference between two electron $\varepsilon_k - \varepsilon_{k+q} \sim 0$. In such a case, the effective attractive electron-phonon interaction

$$V_{q,\nu}^{ep} = -1/N_0 \int_0^\infty \lambda_{q,\nu}^{ph}(\omega) d\omega = -4\gamma_{q,\nu} / (\pi N_0^2 \omega_{q,\nu}^2). \quad (2)$$

From Figs. 2(a)-(c), one can find that some optical modes have large linewidth $\gamma_{q,\nu}$ for all three cases. The relevant frequency $\omega_{q,\nu}$, however, is very high. From Eq. (2), the $V_{q,\nu}^{ep}$ from the optical modes can be neglected. The dramatic difference occurs for the longitudinal acoustic mode. One can find that the electron doping can greatly enlarge the linewidth $\gamma_{q,\nu}$ and soften the frequency $\omega_{q,\nu}$ at the specific momentum $q = \{Q, Q_1\}$. If we plot the phonon spectrum $\omega_{q,\nu}$ and linewidth $\gamma_{q,\nu}$ along different lines, as shown in Figs. 3(a1), (b1) and (c1), one can find another two Q_2 and Q_3 soft mode phonons. Therefore, the $V_{q,\nu}^{ep}$ is

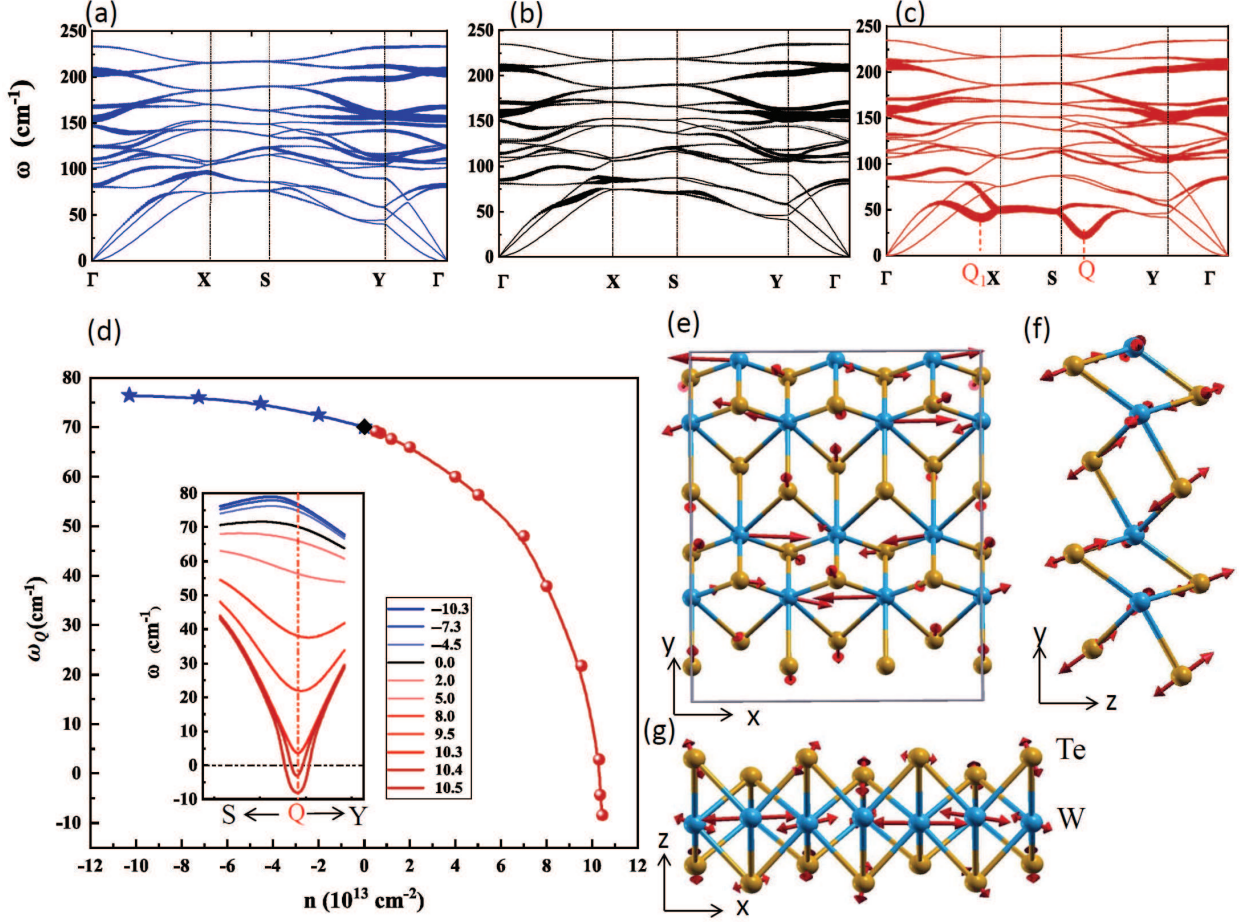


FIG. 2: (Color online) (a)-(c) Calculated phonon spectra for *h*-doped (blue lines), un-doped (black lines), and *e*-doped (red lines) monolayer 1T'-WTe₂, respectively. The linewidth of the spectra is indicated by the weight of the curves. Two characteristic phonon modes at $Q = (\frac{19}{50}, \frac{1}{2})$ and $Q_1 = (\frac{19}{50}, 0)$. The carrier concentration of holes and electrons are $\mp 9.5 \times 10^{13} \text{cm}^{-2}$, respectively. (d) The frequency of *Q* mode as a function of carrier concentration of electrons (red ball) and holes (blue star). The inset figure is used to depict the transition of the *Q* mode with different charge densities, and the line color changes from blue (*h*-doped) to red (*e*-doped) and thickness increases with doping level. Atomic displacements of the *Q* soft mode with (e) top view (*xy* plane), (f) front view (*xz* plane) and (g) side view (*yz* plane). The *Q* mode with a 36-atom unit cell (shown in gray) is six times the size of the primitive cell (dotted green lines). Referring to our previous work [18] for the analysis of soft mode.

strongly enhanced by the electron doping at these special momenta. Note that all Q_i with $i = 0, \dots, 3$ have the same horizontal ordinate $Q_{i,x} = \frac{19}{50}$, as shown in Fig. 3(f). This vector is quite close to the nesting vector of the two electron pockets $K - K' = \frac{17}{50}$. Furthermore, the superconductivity requires condition $\varepsilon_k - \varepsilon_{-k+Q_i} \sim 0$ for the two electrons at Fermi surface. In Fig. 3(g) we show the nesting indicated by vectors Q_1 and Q_2 , and find that Q_1 is the best nesting vector. The consistent relationship between the phonon spectra and the electronic structure indicates that the Fermi surface nesting effect plays the primary role to drive the superconductivity in 1T'-WTe₂.

In Figs. 3(a2)-(e), the calculated $\alpha^2 F(\omega)$ and $\lambda^{ph}(\omega)$ are plotted. In the electron-doped regime, $\alpha^2 F(\omega)$ shows the enhanced sharp peaks at low frequencies in comparison with the un-doped and hole-doped cases. Correspondingly, $\lambda^{ph}(\omega)$ is strongly enhanced in the electron-doped regime. These behaviors are consistent with the above momentum, frequency and mode resolved analyses. To further explore the relation of these soft modes and EPC, we calculate the logarithmic average frequency (ω_{\log}) by averaging over all phonon modes weighted by the $\alpha^2 F(\omega)$:

$$\omega_{\log} = \exp \left[\frac{2}{\lambda^{ph}} \int_0^\omega \frac{\alpha^2 F(\omega) \ln \omega}{\omega} d\omega \right]. \quad (3)$$

The calculated data of ω_{\log} as a function of carrier density n are shown in Fig. 4(a). Clearly, with increasing density of electrons, the ω_{\log} decreases to the low-frequency energy, and the exponential decay trend of ω_{\log} is similar to that of ω_Q as shown in Fig. 2(d). Furthermore, EPC constant λ^{ph} versus charge density n is also plotted in Fig. 4(b), and the data of λ^{ph} are fitted as an exponential growth function excellently. This illustrates the nonlinear enhancement of EPC by soft mode phonons in electron-doped WTe₂, and again proves the electron-hole doping asymmetry of superconductivity in monolayer 1T'-WTe₂, which is different from the doped graphene [20] or doped antimonene [21].

Furthermore, we calculate the T_c with different doping levels using the McMillan-Allen-Dynes formula [22]. The calculated results (data points) of T_c as a function of carrier density of electrons (red ball) and holes (blue star) are plotted in Fig. 4(d). Clearly, compared to the hole doping, the electron doping indeed strengthens the T_c of monolayer 1T'-WTe₂, showing significant asymmetry features, which verifies our previous speculation. More interestingly, T_c reaches the maximum of 3.3 K with $n = 9.5 \times 10^{13} \text{ cm}^{-2}$ (labeled as n_c) corresponding to the best nesting condition, then drops, and finally disappears or merge

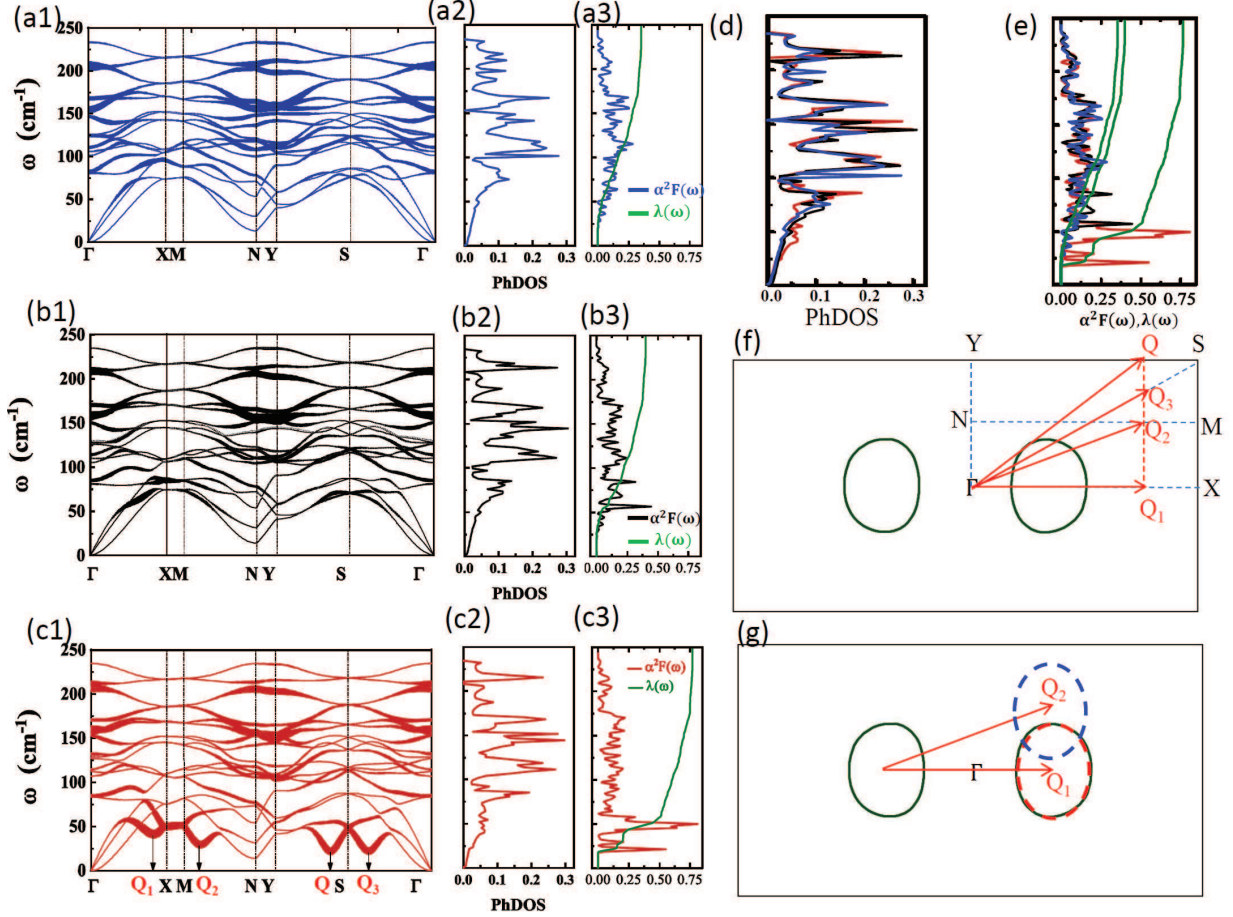


FIG. 3: (Color online)(a1)-(a3)The phonon spectra with linewidth, the phonon density of states, the Eliashberg spectral function $\alpha^2F(\omega)$ and the electron-phonon coupling constant $\lambda(\omega)$ for h -doped monolayer $1T'$ -WTe₂, respectively. (b1)-(b3) and (c1)-(c3) correspond to (a1)-(a3), but for the undoped and e -doped cases, respectively. (d) The plotting of phonon density of states include (a2), (b2) and (c2) for comparison. (e)The plotting of $\alpha^2F(\omega)$ and $\lambda(\omega)$ include (a3), (b3) and (c3) for comparison. (f) The four characteristic phonon modes labeled by Q , Q_1 , Q_2 and Q_3 with $Q_2 = (\frac{19}{50}, \frac{1}{4})$ and $Q_3 = (\frac{19}{50}, \frac{19}{50})$. (d) The Fermi surface nesting indicated by the vectors Q_1 and Q_2 .

into the possible charge density wave instability. The relevant phase diagram is also plotted in Fig. 4(d), from which a superconducting dome can be found. Currently, using solid-state gates or ionic-liquid gates, typical carrier concentration (10^{14} cm^{-2}) can be achieved in several two-dimensional (2D) materials [23–27], we thus expect that future experiments for electron-doped $1T'$ -WTe₂ can verify our maximum T_c (3.3 K), which is about four or

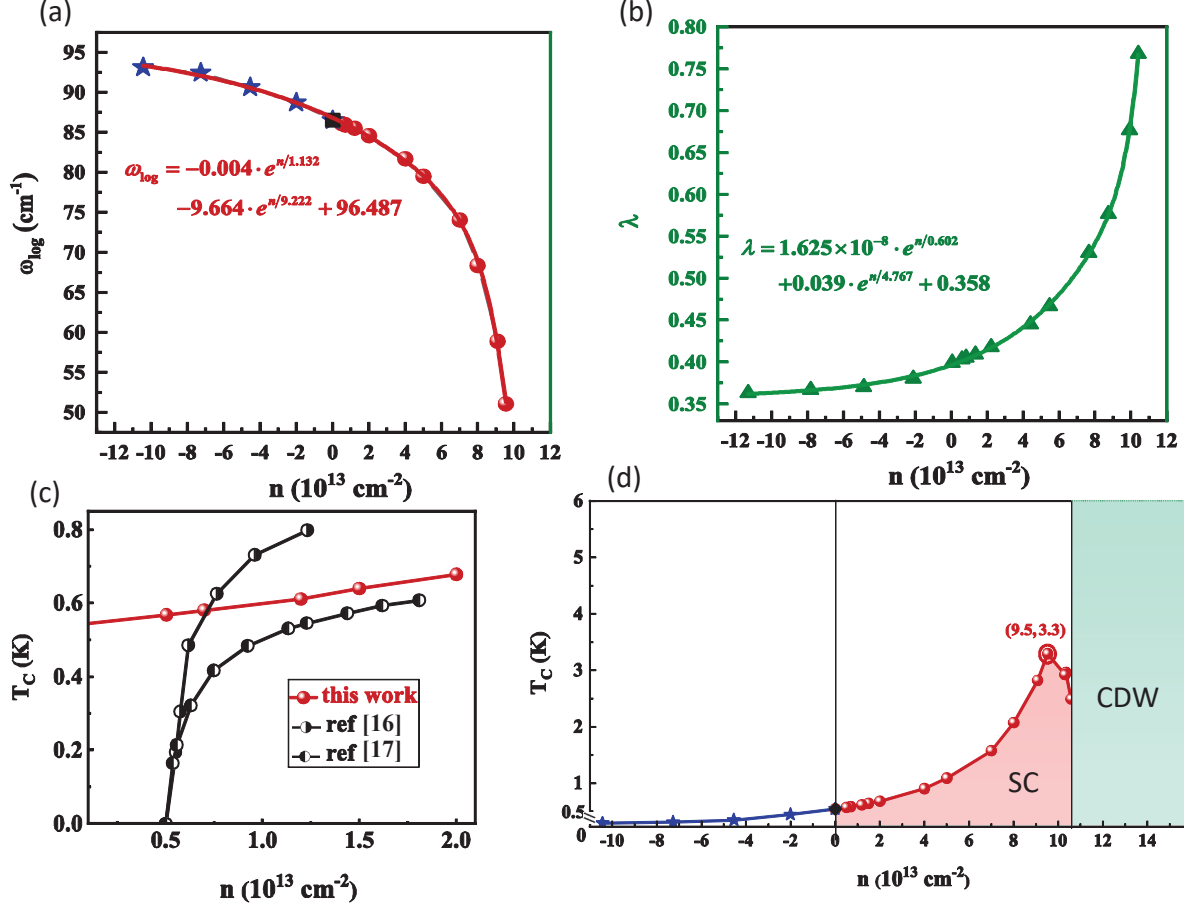


FIG. 4: (Color online) (a) and (b) ω_{\log} and λ as a function of n , respectively. The red line and green line are well fit to the data of ω_{\log} and λ as an exponential function, respectively. (c) A comparison between our calculation with the experimental results [16, 17] for e -doped $1T'$ - WTe_2 . The logarithmical T_c from [16] has been converted. (d) A $T_c - n$ phase diagram is plotted. The boundary of solid line with small balls are given by our calculations. SC and CDW label superconducting phase and charge density wave state, respectively.

five times the experimental values of 0.8 K [16] or 0.6 K [17]. In the range of experimental charge concentration, i.e., $n \in [0.7, 2.1] \times 10^{13} \text{cm}^{-2}$, our results are in qualitative agreement with the experimental values [16, 17], as shown in Fig. 4(c).

Now, we turn to understand the superconducting properties of monolayer $1T'$ - WTe_2 in the electron-doped regime. According to Fig. 1(e), there exist two separated Fermi pockets centered at momenta \mathbf{K}' and \mathbf{K} which can be regarded as two valleys. The low-energy Hamiltonian can be expanded around \mathbf{K}' and \mathbf{K} . Define the annihilation electron operator

TABLE I: Classification of the inter-valley s -wave pairings according to the representations of C_{2h} point group.

	$C_2(z)$	σ_h	i	$\hat{\Delta}$	$\hat{\Delta}$
IR	$s_z\tau_x$	$-is_z$	τ_x	Matrix form	Explicit form
A_g	1	1	1	τ_x	$c_{+\uparrow}c_{-\downarrow} - c_{+\downarrow}c_{-\uparrow}$
B_u	-1	1	-1	$s_z\tau_y$	$c_{+\uparrow}c_{-\downarrow} + c_{+\downarrow}c_{-\uparrow}$
A_u	1	-1	-1	$s_x\tau_y$	$c_{+\uparrow}c_{-\uparrow} - c_{+\downarrow}c_{-\downarrow}$
				$s_y\tau_y$	$i(c_{+\uparrow}c_{-\uparrow} + c_{+\downarrow}c_{-\downarrow})$

as $c_{\mathbf{k},\eta,s}$, where \mathbf{k} is the momentum measured from \mathbf{K}' and \mathbf{K} , $\eta = \pm$ is for two valleys and $s = \uparrow, \downarrow$ is for spin. On the basis of $[c_{\mathbf{k},+\uparrow}, c_{\mathbf{k},-\uparrow}, c_{\mathbf{k},+\downarrow}, c_{\mathbf{k},-\downarrow}]$, the effective Hamiltonian is

$$\mathcal{H}_0 = (\varepsilon_k - \mu)s_0\tau_0 + g\mu_B\tau_0\mathbf{B} \cdot \mathbf{s}. \quad (4)$$

Here, s and τ are two sets of Pauli matrices for spin and valley degrees of freedom, $\varepsilon_k = \hbar^2k^2/2m - \mu$ is the dispersion with the chemical potential μ , g and μ_B are the Lande g factor and Bohr magneton, respectively, and $\mathbf{B} = (B_x, B_y, B_z)$ is the external magnetic field. Note that we only take into account the Zeeman effect of the external magnetic field, but neglect the orbital effect due to the 2D feature of 1T'-WTe₂. In the superconducting states, the pairings should follow the IRs of the C_{2h} point group of 1T'-WTe₂. In order to consider the superconductivity for simplicity, we adopt the approximation of Fermi surface average of $V_{q,\nu}^{ep}$ to neglect the weak momentum dependence, *i.e.*, $V^{ep} = \sum_{\nu} \langle V_{\mathbf{k}-\mathbf{k}',\nu}^{ep} \rangle_{\mathbf{k},\mathbf{k}' \in FS}$. Thus, we only consider the momentum-independent s -wave pairings, with the constant pairing interaction $-V_0 = V^{ep} + U_{scou}$ with U_{scou} the screen Coulomb interaction. Furthermore, the soft-mode phonons have the momenta connecting the two valleys, which indicates only the inter-valley pairing is possible. Under the mean-field approximation in the Nambu basis, we can classify the pairing symmetry under the constraint of anticommutation relation between fermion operators. The pairing function can be parameterized by the form $\hat{\Delta} = \sum_i \Delta_i \Gamma_i$, where Γ_i is the i th IR matrix product from s and τ . The results are listed in Table I. The pairing interaction in all pairing channels in Table I has the same amplitude of $V_0/2$.

To evaluate the possible superconducting pairing in 1T'-WTe₂, we solve the following linearized gap equations for T_c in each pairing channel [28, 29]

$$V_0\chi_i/2 = 1, \quad (5)$$

where χ_i is the finite temperature superconducting susceptibility in i th pairing channel, and can be calculated by

$$\chi_i = -\frac{1}{\beta} \sum_{i\omega_n, k} \text{Tr}[\Gamma_i^\dagger \mathcal{G}_e(k, i\omega_n) \Gamma_i \mathcal{G}_h(k, i\omega_n)]. \quad (6)$$

Here, $\mathcal{G}_{e/h}(k, i\omega_n) = [i\omega_n \mp \mathcal{H}_0(k)]^{-1}$ are the relevant standard electron and hole Matsubara Green functions. Note that only the electron-type bands are taken into account in the electron-doped regime. With the approximation that the pairing occurs at the Fermi surface, we can get $\chi_{A_g} = 4\chi_0$, $\chi_{B_u} = 4\chi_0 B_z^2/B^2$, $\chi_{A_u} = 4\chi_0 B_x^2/B^2$ or $4\chi_0 B_y^2/B^2$. $\chi_0 = N_0 \int d\varepsilon \tanh(\frac{\varepsilon}{2k_B T})/\varepsilon$ is the standard superconducting susceptibility and k_B is the Boltzmann constant. When $\mathbf{B} = 0$, one can find that all the pairing channels have the same superconducting susceptibility, i.e., $4\chi_0$, likewise, the same T_c , i.e., $k_B T_c = \frac{2e^\gamma}{\pi} \hbar \omega_D \exp(-\frac{1}{2N_0 V_0})$, where $\gamma \approx 0.5772$ is the Euler constant and ω_D is the Debye frequency. It indicates that all the pairing channels are degenerate and are the possible candidate for the superconducting ground state. When $\mathbf{B} \neq 0$, the T_c of A_g channel is robust against the magnetic field. The T_c of B_u or A_u channel is magnetic-field-direction dependent. Namely, $\ln \frac{T_{c, B_u}(B)}{T_{c, B_u}(0)} = \frac{1}{2N_0 V_0} (1 - \frac{B^2}{B_z^2})$ and $\ln \frac{T_{c, A_u}(B)}{T_{c, A_u}(0)} = \frac{1}{2N_0 V_0} (1 - \frac{B^2}{B_{x/y}^2})$. Therefore, the B_u channel is robust against the out-of-plane magnetic field $B = (0, 0, B_z)$ and is fragile for the in-plane magnetic field $B = (B_x, B_y, 0)$. In other words, B_u channel has large $H_{c2, \perp}$ and small $H_{c2, \parallel}$. Similarly, one can find A_u channel has small $H_{c2, \perp}$ and large $H_{c2, \parallel}$. In comparison with the experimental observations, we find that the superconducting states in monolayer 1T'-WTe₂ should fall into the A_u channel with the qaual-spin-triplet pairing, whose upper critical field cannot be restricted by the Pauli paramagnetic limit. These results can be easily understood through the spin structure of the Cooper pairs. The B_u and A_u correspond to the three components S_z and S_x, S_y of the $S = 1$ spin-triplet Cooper pairs, respectively. Therefore, the couplings between them and the magnetic field follow the Zeeman-type to minimize the ground state energy. For a general magnetic field with $B = B_0(\cos \theta \cos \varphi, \cos \theta \sin \varphi, \sin \theta)$, we can get the exact pairing form as $\hat{\Delta} \sim e^{i\varphi} c_{\mathbf{k}, +\uparrow} c_{-\mathbf{k}, -\uparrow} - e^{-i\varphi} c_{\mathbf{k}, +\downarrow} c_{-\mathbf{k}, -\downarrow}$, where the phase φ is determined by the direction of magnetic field.

There exist several other mechanisms to result in the strongly anisotropic upper critical

magnetic field H_{c2} including type-I [26, 30, 31], type-II Ising pairings [32] and spin-orbit scattering [33]. Type-I Ising pairing mechanism is related to inversion symmetry breaking and clearly is not the case in monolayer 1T'-WTe₂, which preserves the inversion symmetry. Type-II Ising pairing mechanism relies on the band near Γ point with out-of-plane orientation of the spin locked by the spin-orbit coupling. This mechanism can also be excluded, because no such kind of band splitting exists in monolayer 1T'-WTe₂. For the spin-orbit scattering mechanism, there are two kinds of situations. In the clean limit of crystalline sample with high mobility, the spin-orbit coupling scattering can be discarded as it could induce the unphysically short scattering times [26, 30, 31]. In the dirty limit, the strong spin-orbit coupling indeed could induce the strongly anisotropic H_{c2} . However, the superconductivity refers to the Fermi surface connected by the momenta relating to soft phonons. From Fig. 1 (b), the pieces of the Fermi surface close to the X point mainly has the $5d$ orbital characters of W, which means the weak spin-orbit coupling therein [34]. This is also the reason why the simple low-energy Hamiltonian in Eq. (4) is enough and is adopted to investigate the properties of superconducting state in monolayer 1T'-WTe₂. Thus, the spin-orbit scattering mechanism can be excluded.

In conclusion, we have determined the emergence of soft-mode phonons, the relevant enhanced electron-phonon coupling and the Fermi surface nesting is the mechanism of superconductivity of monolayer 1T'-WTe₂ in the electron-doped regime. A superconducting dome is obtained in the phase diagram. An unconventional superconducting pairing with equal spin triplet in A_u channel is proposed to capture the experimentally observed strong in-plane and weak out-of-plane upper critical fields.

Acknowledgments

This work was financially supported by the National Key R&D Program of China No. 2017YFA0303201, National Natural Science Foundation of China under Grants (No. 11625415, No. 61605014, No. 11674331), the ‘‘Strategic Priority Research Program (B)’’ of the Chinese Academy of Sciences, Grant No. XDB33030100, the ‘100 Talents Project’ of the Chinese Academy of Sciences, CASHIPS Director’s Fund (BJPY2019B03), the Science Challenge Project under Grant No. TZ2016001. A portion of this work was supported by

the High Magnetic Field Laboratory of Anhui Province, China.

- [1] Y. S. Hor, A. J. Williams, J. G. Checkelsky, P. Roushan, J. Seo, Q. Xu, H. W. Zandbergen, A. Yazdani, N. P. Ong, and R. J. Cava, *Phys. Rev. Lett.* **104**, 057001 (2010).
- [2] Z. Liu, X. Yao, J. Shao, M. Zuo, L. Pi, S. Tan, C. Zhang, and Y. Zhang, *J. Am Chem. Soc.* **137**, 10512 (2015).
- [3] M. P. Smylie, K. Willa, H. Claus, A. Snezhko, I. Martin, W.-K. Kwok, Y. Qiu, Y. S. Hor, E. Bokari, P. Niraula, A. Kayani, V. Mishra, and U. Welp, *Phys. Rev. B* **96**, 115145 (2017).
- [4] T. Asaba, B. J. Lawson, C. Tinsman, L. Chen, P. Corbae, G. Li, Y. Qiu, Y. S. Hor, L. Fu, and L. Li, *Phys. Rev. X* **7**, 011009 (2017).
- [5] K. Kirshenbaum, P. S. Syers, A. P. Hope, N. P. Butch, J. R. Jeffries, S. T. Weir, J. J. Hamlin, M. B. Maple, Y. K. Vohra, and J. Paglione, *Phys. Rev. Lett.* **111**, 087001 (2013).
- [6] C. Zhang, L. Sun, Z. Chen, X. Zhou, Q. Wu, W. Yi, J. Guo, X. Dong, and Z. Zhao, *Phys. Rev. B* **83**, 140504(R) (2011).
- [7] L. Fu and C. L. Kane, *Phys. Rev. Lett.* **100**, 096407 (2008).
- [8] R. M. Lutchyn, J. D. Sau, and S. D. Sarma, *Phys. Rev. Lett.* **105**, 077001 (2010)
- [9] J. Xu, C. Liu, M. Wang, J. Ge, Z. Liu, X. Yang, Y. Chen, Y. Liu, Z. Xu, C. Gao, D. Qian, F. Zhang, and J. Jia, *Phys. Rev. Lett.* **112**, 217001 (2014).
- [10] N. Hao and J. Hu, *Natl. Sci. Rev.* **6**, 213 (2019).
- [11] H. Wang, L. Ma, and J. Wang, *Sci. Bull.* **63**, 1141 (2018).
- [12] H. Wang, H.-C. Wang, H.-W. Liu, H. Lu, W.-H. Yang, S. Jia, X.-J. Liu, X.-C. Xie, J. Wei, and J. Wang, *Nat. Mater.* **15**, 38 (2016).
- [13] L. Aggarwal, A. Gaurav, G. S. Thakur, Z. Haque, A. K. Ganguli, and G. Sheet, *Nat. Mater.* **15**, 32 (2016).
- [14] X.-Y. Hou, Z. Wang, Y.-D. Gu, J.-B. He, D. Chen, W.-L. Zhu, M.-D. Zhang, F. Zhang, Y.-F. Xu, S. Zhang, H.-X. Yang, Z.-A. Ren, H.-M. Weng, N. Hao, W.-G. Lv, J.-P. Hu, G.-F. Chen, and L. Shan, *Phys. Rev. B* **100**, 235109 (2019).
- [15] X.-Y. Hou, Y.-D. Gu, S.-J. Li, L.-X. Zhao, W.-L. Zhu, Z. Wang, M.-D. Zhang, F. Zhang, L. Zhang, H. Zi, Y.-W. Wu, H.-X. Yang, Z.-A. Ren, P. Zhang, G.-F. Chen, N. Hao, and L. Shan, *Phys. Rev. B* **101**, 134503 (2020).

- [16] E. Sajadi, T. Palomaki, Z. Fei, W. Zhao, P. Bement, C. Olsen, S. Luescher, X. D. Xu, J. A. Folk and D. H. Cobden, *Science* **362**, 922 (2018).
- [17] V. Fatemi, S. F. Wu, Y. Cao, L. Bretheau, Q. D. Gibson, K. Watanabe, T. Taniguchi, T. J. Cava, and P. Jarillo-Herrero, *Science* **362**, 926 (2018).
- [18] W. Yang, Z. Y. Yuan, Y. Q. Luo, Y. Yang, F. W. Zheng, Z. H. Hu, X. H. Wang, Y. A. Liu, and P. Zhang, *Phys. Rev. B* **99**, 235401 (2019).
- [19] P. B. Allen, *Phys. Rev. B* **6**, 2577 (1972).
- [20] C. Si, Z. Liu, W. H. Duan, and F. Liu, *Phys. Rev. Lett.* **111**, 196802 (2013).
- [21] A. V. Lugovskoi, M. I. Katsnelson, and A. N. Rudenko, *Phys. Rev. B* **99**, 064513 (2019).
- [22] P. B. Allen and R. Dynes, *Phys. Rev. B* **12**, 905 (1975).
- [23] Y. J. Fu, E. Liu, H. T. Yuan, P. Z. Tang, B. Lian, G. Xu, J. W. Zeng, Z. Y. Chen, Y. J. Wang, W. Zhou, K. Xu, A. Y. Gao, C. Pan, M. Wang, B. G. Wang, S. C. Zhang, Y. Cui, H. Y. Hwang, and F. Miao, *NPJ Quantum Mater.* **2**, 52 (2017).
- [24] L. J. Li, E. C. T. O’Farrell, K. P. Loh, G. Eda, B. Öyilmaz, and A. H. Castro neto, *Nature* **529**, 185 (2016).
- [25] Y. Saito, T. Nojima, and Y. Iwasa, *Supercond. Sci. Tech.* **29**, 093001 (2016).
- [26] J. M. Lu, O. Zheliuk, I. Leermakers, N. F. Q. Yuan, U. Zeitler, K. T. Law, and J. T. Ye, *Science* **350**, 1353 (2015).
- [27] D. Costanzo, S. Jo, H. Berger, and A. F. Morpurgo, *Nat. Nanotech.* **11**, 339 (2016).
- [28] L. Fu and E. Berg, *Phys. Rev. Lett.* **105**, 097001 (2010).
- [29] C. Liu, *Phys. Rev. Lett.* **118**, 087001 (2010).
- [30] Y. Saito, Y. Nakamura, M. S. Bahramy, Y. Kohama, J. Ye, Y. Kasahara, Y. Nakagawa, M. Onga, M. Tokunaga, T. Nojima, Y. Yanase, and Y. Iwasa, *Nat. Phys.* **12**, 144–149 (2016).
- [31] X. Xi, Z. Wang, W. Zhao, J. Park, K. T. Law, H. Berger, L. Forró, J. Shan, and K. F. Mak, *Nat. Phys.* **12**, 139–143 (2016).
- [32] J. Falson, Y. Xu, M. Liao, Y. Zang, K. Zhu, C. Wang, Z. Zhang, H. Liu, W. Duan, K. He, H. Liu, J. H. Smet. D. Zhang, and Q.-K. Xue, *Science*, aax3873 (2020).
- [33] R. A. Klemm, A. Luther, and M. R. Beasley, *Phys. Rev. B* **12**, 877 (1975).
- [34] X. Qian, J. Liu, L. Fu, and J. Li, *Science* **346**, 1344 (2014).